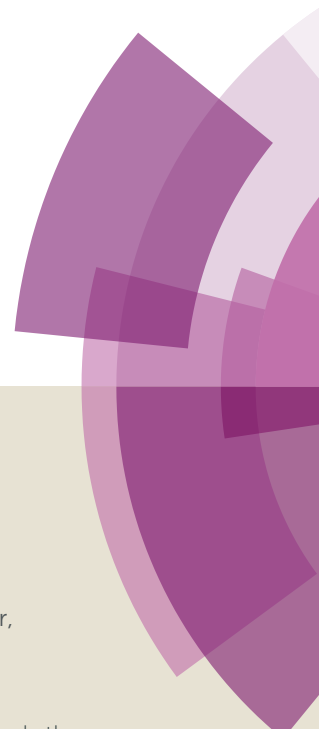
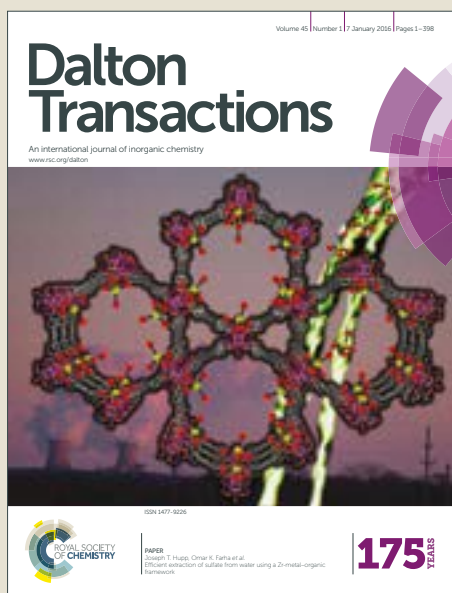


Dalton Transactions

Accepted Manuscript



This article can be cited before page numbers have been issued, to do this please use: M. Godino-Ojer, A. López-Peinado, F. J. Maldonado Hodar, E. Bailón-García and E. Perez-Mayoral, *Dalton Trans.*, 2019, DOI: 10.1039/C8DT04403A.



This is an Accepted Manuscript, which has been through the Royal Society of Chemistry peer review process and has been accepted for publication.

Accepted Manuscripts are published online shortly after acceptance, before technical editing, formatting and proof reading. Using this free service, authors can make their results available to the community, in citable form, before we publish the edited article. We will replace this Accepted Manuscript with the edited and formatted Advance Article as soon as it is available.

You can find more information about Accepted Manuscripts in the [author guidelines](#).

Please note that technical editing may introduce minor changes to the text and/or graphics, which may alter content. The journal's standard [Terms & Conditions](#) and the ethical guidelines, outlined in our [author and reviewer resource centre](#), still apply. In no event shall the Royal Society of Chemistry be held responsible for any errors or omissions in this Accepted Manuscript or any consequences arising from the use of any information it contains.

Cobalt oxide-carbon nanocatalysts with highly enhanced catalytic performance for the green synthesis of nitrogen heterocycles through Friedländer condensation

Marina Godino-Ojer,^{a,b} Antonio J. López Peinado,^a Francisco J. Maldonado-Hódar,^{c*} Esther Bailón-García^c and Elena Pérez Mayoral^{a*}

Received 00th January 20xx,
Accepted 00th January 20xx

DOI: 10.1039/x0xx00000x

www.rsc.org/

Novel series of eco-sustainable catalysts developed by supporting CoO-nanoparticles on different carbon supports, highly efficient in the synthesis quinolines and naphthyridines, through the Friedländer condensation, are reported for the first time. Textural properties, dispersion and location of the Co-phase are influenced by the nature of carbon support, Co-precursor salt and metal loading, having an important impact on the catalytic performance. Thus, the presence of the meso- and macropores in carbon aerogels together the homogenous distribution of the active phase favours the formation of the product **3a** as function of the metal loading. However, the increase of the metal content when using CNTs implies the formation of CoO aggregates and an optimal concentration of 3% wt CoO was observed providing the highest conversion values. The carbon-based catalysts herein reported can be considered a sustainable alternative showing advantages such as easy preparation, superior stability and notably enhanced catalytic performance, operating at lower temperature and under solvent-free conditions.

Introduction

Development of new catalytic technologies by using carbon materials constitutes a currently hot topic. Nanocarbons as their different forms could be considered almost ideal supports for catalytic purposes due to their unique characteristics such as high surface areas, chemical inertness and thermal stability, among others, providing the appropriate chemical environment to produce fine chemicals.^{1,2} In the last decades metal-supported carbon-based materials applied in catalysis have particularly attracted much attention.³ Activated carbons (ACs) have been used in catalysis for a long time.⁴ However, the application of nanostructured carbon forms such as carbon nanotubes (CNTs) and more recently carbon aerogels⁵ are issues of interest and continuously growing. For instance, Pd/Co nanoparticles supported on multi-walled CNTs have recently reported in the microwave-assisted efficient synthesis of substituted tetrazoles⁶, Cu loadings on Ni/carbon nanotubes catalysts in the hydrodeoxygenation reaction of guaiacol⁷, and RuCNT nanohybrid in the selective catalytic reduction of nitrochalcones to quinoline N-oxides⁸. AuCNTs have been also found to be interesting catalysts in diverse

chemical transformations such as oxidation reaction of silanes⁹, alcohols¹⁰ and in the synthesis of quinoxalines¹¹ among others. More recently, cobalt-carbon composites have been applied in the reduction of *p*-nitrophenol and pendimethaline¹² and as electrocatalysts for oxygen evolution reactions¹³.

Graphene based materials have been also used in catalysis¹⁴, particularly graphene supported metal/metal oxide hybrids applied in fine chemical synthesis¹⁵. For instance, Ru or Rh nanoparticles supported on graphene¹⁶ and cobalt nanoparticles encapsulated in porous nitrogen-doped graphene¹⁷ have been reported for the hydrocarbon hydrogenation and chemoselective hydrogenation of quinolines, respectively.

As one of our research lines, we have developed different environmental-friendly and efficient methodologies for the synthesis of quinolines, through Friedländer condensation¹⁸, involving acid and basic activated carbons¹⁹⁻²⁰ and much more recently metal-free carbon aerogels²¹ and transition metal doped carbon aerogels²²⁻²³. As far as we know, our studies represent the first examples of transition metal doped carbon aerogels implied in the aldol-based reactions, demonstrating that Co⁰ or Cu⁰ nanoparticles over the surface on carbon aerogels are the main active catalytic species producing quinolines in high yields.

With these items in mind, the goal of this paper is aimed onto the comparative study of using three types of carbon forms in the synthesis of quinolines and related compounds, *via*

^a Departamento de Química Inorgánica y Química Técnica, Universidad Nacional de Educación a Distancia, UNED, Paseo Senda del Rey 9, Facultad de Ciencias, 28040, (Madrid, Spain).

^b Facultad de Ciencias Experimentales, Universidad Francisco de Vitoria, UFV, Ctra. Pozuelo-Majadahonda km 1.800, 28223, Pozuelo de Alarcón (Madrid, Spain).

^c Departamento de Química Inorgánica, Universidad de Granada, UGR, Facultad de Ciencias, 18071, (Granada, Spain)

Friedländer reaction, in which Co nanoparticles are supported. The carbon-based materials of our choice are a carbon aerogel B-500, commercial AC, Norit RX 3, and multiwall carbon nanotubes (MWCNTs) showing different morphologies and textures. While Norit RX 3 AC is mainly a microporous sample, the B-500 aerogel shows a mesoporous character. It is noticeable that the polymerization resorcinol-formaldehyde (R-F) leading to nanostructured carbon gels allows the control of the porosity and morphology of these materials as well as of their tuned surface chemistry. In fact, the relationship of the surface properties and the catalytic behaviour of these nanocarbons are continuously revised hot topics in this field.⁵ In this work, we seek to develop a novel sustainable series of carbon-based Co catalysts with enhanced catalytic performance. At this regard, the relationship between the morphology, textural properties of the different carbon samples and the effect of the concentration and dispersion of active phases onto the catalysts and the catalytic performance are envisioned.

Materials and Methods

Synthesis and characterization of the nanocatalysts

Three series of Co-catalysts were prepared by impregnation of different types of carbon materials with cobalt salts. Commercial AC Norit RX3 and MWCNTs have been purchased from NORIT Nederland B.V. and Sigma-Aldrich, respectively. Norit RX3 was milled and sieved to a particle size below 0.25 mm, without any chemical treatment. However, MWCNTs were firstly treated with concentrated HNO₃, under refluxing conditions, according the experimental protocol reported by Trépanier et al.²⁴ B500 carbon aerogel was synthesized in our laboratories from resorcinol (R) and formaldehyde (F) polymerization. The experimental protocol for the synthesis was reported elsewhere.^{5,25} In this case, resorcinol (R), formaldehyde (F) (molar ratio R/F = 1:2) and Na₂CO₃ (C) (R/C = 300) were dissolved in water (W) and cast into glass moulds (25 cm length x 0.5 cm internal diameter). After the curing period (1 day at room temperature, 2 days at 303 K and 5 days at 353 K), the gel rods were cut in 5 mm pellets, exchanged with acetone and supercritically dried with carbon dioxide. B500 carbon aerogel was obtained by carbonization of this organic aerogel at 773 K in N₂ flow in a tubular furnace using a temperature ramp of 1.5 K/min and a soak time of 2h. No activating agents were applied. The final carbonized is milled and sieved also below 0.25 mm.

The cobalt-supported catalysts were prepared by treatment of the different carbon materials with the appropriate aqueous solution of cobalt nitrate (Co(NO₃)₂) or cobalt acetate, ((CH₃CO₂)₂Co), to obtain the corresponding Co-loading. Briefly, carbon supports (5 g) were impregnated with differently concentrated Co(NO₃)₂ water solutions (25 mL). The used Co(NO₃)₂·6H₂O amounts were 0.247, 0.741, and 1.235 g corresponding to 1, 3 and 5% wt. After drying overnight at 383 K, the samples were pre-treated in He-flow at 573 K to obtain the Co active phase. Similar protocol was performed for the

(CH₃CO₂)₂Co impregnated samples by using the appropriated cobalt salt amounts. Three catalyst series Co-NT_n, Co-B500-NC_n and NoritCo were obtained, where n is the theoretic Co loading expressed as % wt. Samples in which the cobalt salt for impregnation was (CH₃CO₂)₂Co were marked using Ac notation.

The morphology of carbons was analysed using a scanning electron microscope (Leo, Carl Zeiss, Gemini-153). Images were obtained at excitation energy of 20 kV. The textural characteristics of the samples were obtained by mercury porosimetry and gases adsorption. The macro-mesoporosity of the samples was analysed by mercury porosimetry (Autoscan60 from Quantachrome). The sorption isotherms of N₂ and CO₂ at 77 and 273 K were determined using an Autosorb 1 from Quantachrome after outgassing samples overnight at 383 K under high vacuum (10⁻⁶ mbar). Parameters as BET surface area and micropore volume (W₀) were calculated by applying respectively the BET or Dubinin-Radushkevich equations to the isotherms.^{26,27} The pore size distributions (PSD) were determined by applying Quenched Solid Density Functional Theory (QSDFT), assuming slit-shaped pores, to the N₂ sorption isotherms.²⁸ The total pore volume (V_T) is considered as the volume of adsorbed nitrogen at a relative pressure P/P₀ = 0.95.²⁹

Thermal treatments of samples were simulated by thermogravimetric analysis using a SHIMADZU mod. TGA-50H for TG-DTG experiments. The metal content of the supported catalysts was obtained by burning a fraction of it in the thermobalance, at 1123 K, under air flow up to constant weight. Thermal Programmed Desorption (DTP) curves of carbon monoxide, carbon dioxide, water and hydrogen were recorded. Experiments were carried out by heating 150 mg of sample at 303 K/min up to 1273 K using He as the carrier gas (60 cm³/min). The analysis of desorbed gases was performed with a Mass Spectrometer model Prisma (Pfeiffer).

The chemical nature and dispersion of the metal were studied by X-ray diffraction (XRD, Phillips PW1710 diffractometer), high-resolution transmission electron microscopy (HRTEM, Phillips CM-20 or HAADF FEI TITAN G2 microscope) equipped with FEI system of EDX analysis. More than 100 metal nanoparticles were analysed in each case from the corresponding microphotographs using the appropriate software (ImageJ) where a mean diameter is calculated. The equivalent metallic particles were determined taking into account the densities of metal and oxide³⁰⁻³³. The Co-dispersion was calculated from this average particle size by applying the equation: $D = 96/d(\text{nm})$ assuming spherical particles and a homogeneous density sites of 14.6 atoms nm⁻². X-ray photo emission spectra (XPS) were recorded using a Kratos Axis Ultra-DLD spectrometer. This instrument utilizes as the radiation source Mg K α (1253.6 eV) and a hemispheric electron analyser operating at 12 kV and 10 mA.

Catalytic performance

In a typical experiment, a mixture of the corresponding 2-aminoaryl aldehyde **1** (0.5 or 2 mmol) and ethyl acetoacetate **2**

(5 mmol) in a three-necked vessel, equipped with thermometer, was placed on a multiexperiment work station StarFish (Radley's Discovery Technologies IUK). When the temperature reaches 303 or 323 K, the catalyst was added (25 mg) and the reaction mixture was stirred during 240 min. The samples were periodically taken at 15, 30, 60, 120, 180 and 240 min, diluted with acetone (0.5 mL), and the catalyst was filtered off and the solvent evaporated in vacuo.

The reactions were followed by TLC chromatography performed on DC-Aulofolien/Kieselgel 60 F245 (Merk) using mixtures of CH₂Cl₂/EtOH 98:2 as eluent. Products were characterized by ¹H NMR spectroscopy. NMR spectra were recorded by using a Bruker AVANCE DPX-300 spectrometer (300 MHz for ¹H). ¹H chemical shifts in [d₆]DMSO are referenced to internal tetramethylsilane.

Yield (or conversion values) is defined as the fraction of reactant **1** transformed at each reaction time into compounds **3** determined by ¹H NMR. The reactions under study yield exclusively compounds **3**, therefore, selectivity being of 100%.

The performance of the investigated catalysts was compared also in terms of specific activity, R – (mmol/g(Co) · s) – and turn over frequencies, TOF – (mol **1a** converted/mol surface-Co · s) –³⁴.

$$\text{TOF (s}^{-1}\text{)} = \text{M1} \cdot \text{X} / (\text{D} \cdot \text{n} \cdot \text{t})$$

Where M1 are the initial mol **1a** reactant, X is the conversion at 15 min for comparison, D is the dispersion, n is the total moles of Co-used and t is the time on stream.

Results and Discussion

View Article Online

DOI: 10.1039/C8DT04403A

Physico-chemical characterization of the carbon catalysts

The physico-chemical properties of the catalysts will be related with the characteristics of supports. Considering that the samples were prepared by impregnation, the metal content obtained by TG for the different catalysts fits according the programed loading. The elemental analysis of CNT_{ox}, B500 and Norit supports and the oxygen content calculated from the DTP experiments are collected in Table 1. Heating in inert atmosphere the weight loss (WL) undergone by the samples corresponds to the amount of gases evolved as CO_x from the decomposition of the oxygenated surface groups (OSG), which can be also characterized as a function of their thermal stability. The higher oxygen content determined by elemental analysis for the Norit support is influenced by ash content of this sample (4.8 %). In fact, the oxygen content determined by DTP is only around 2%. Lower oxygen content is determined for B500 aerogel. In this case, the only oxygen sources are resorcinol and formaldehyde. During the synthesis, methylene-ether links between aromatic rings in the organic aerogels are formed, which evolve during the carbonization process.³⁵ Thus, this sample is obviously ash free, because it is synthesized from pure organic monomers. The corresponding CO and CO₂ DTP profiles are showed in Fig. 1A and 1B. The appearance of different maxima in the profiles confirms the presence of distinct types of OSG with different stability. The first peak at

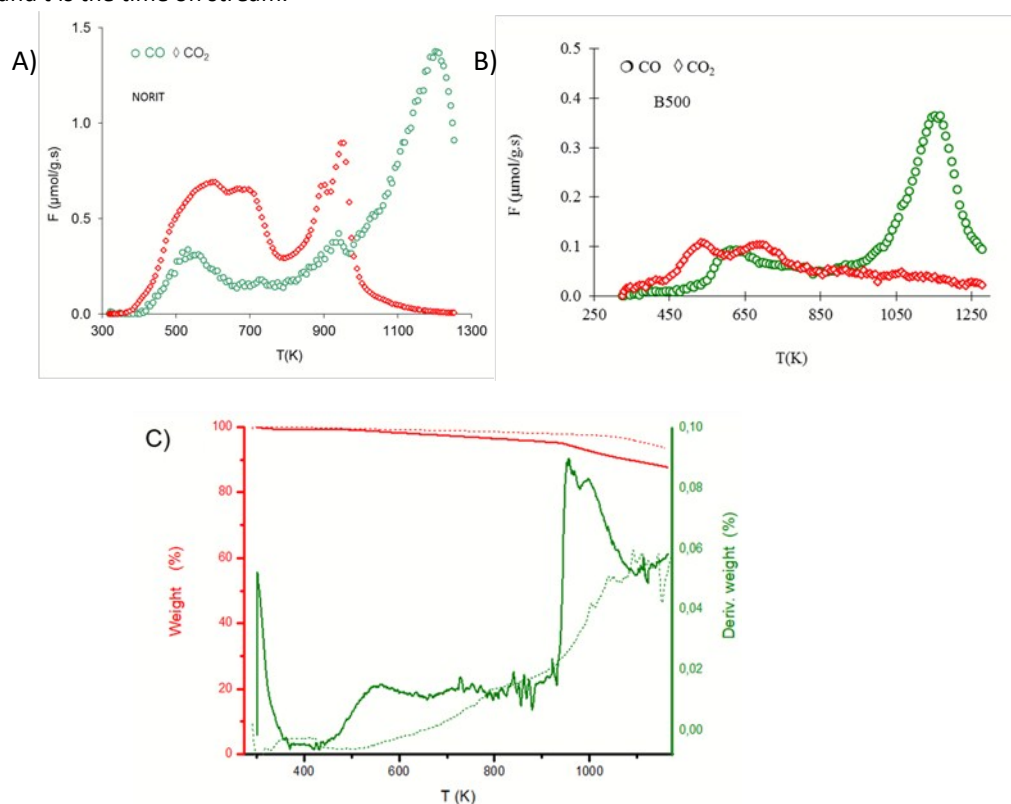


Fig. 1 CO and CO₂ DTP profiles of A) Norit and B) B500 supports C) TG-DTG profiles in He flow of CNT (---) and CNT_{ox} (—) supports

Table 1. Elemental analysis of the supports.

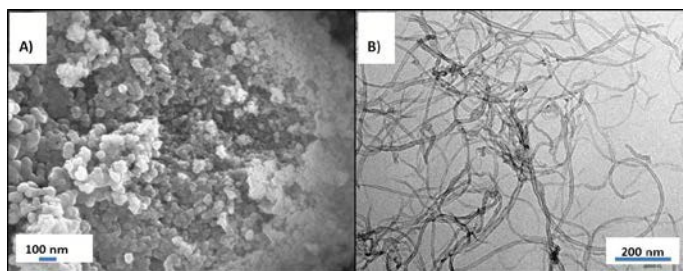
Sample	C (%)	H (%)	N (%)	S (%)	O ^[a] (%)	O _{DTP} (%)
Norit	89.0	0.3	0.7	0.0	11.0	2.8
B500	96.3	0.2	0.0	0.0	3.5	1.2
CNT _{ox}	92.0	0.4	0.2	0.0	7.4	5.1 ^[b]
CNT	94.2	0.5	0.6	0.1	4.7	2.5 ^[b]

^[a] Oxygen content obtained by difference. ^[b] From TG experiments.

low temperature (at around 543 K) corresponds to the evolution of carboxylic acid groups. When increasing temperature, the decomposition of OSG such as anhydrides, formed from dehydration of adjacent carboxylic groups occurs. Mainly in the case of Norit sample there are present other CO₂-evolving groups with higher thermal stability. The peak at around 973 K is associated to the decomposition of lactone groups. In the case of the CO-profile, CO is also formed from anhydride groups (CO + CO₂), and with increasing temperatures from phenol, carbonyl or ether OSG, the latter decomposing at around 1173 K.^{36,37} Similar conclusions that those previously described from DTP were pointed out when analysing the profiles obtained by TG-DTG in He flow (Fig. 1C).

The oxygen content for CNT_{ox} support evidently increases after HNO₃ treatment regarding raw CNT (Table 1), changing also the nature of the OSG. Thus, it is observed that effectively the WL of CNT_{ox} > CNT due to the formation of OSG. The clear maximum at around 550 K observed for CNT_{ox} sample corresponding to the evolution of carboxylic acid groups while the main desorption occurring at around 973 K is associated to the CO evolved from ether or carbonyl groups.

The morphology of the samples was investigated by SEM/TEM (Fig. 2). Figure 2 A corresponds to the well-known structure of aerogel B500 built by aggregation of nearly spherical primary particles. The support CNT_{ox} also maintains evidently the typical morphology of MWCNT (Fig. 2 B) while Norit AC is a particulate material with more or less rough surface (not shown). This morphology is also related with the porosity of the samples.

**Fig. 2** Morphology of A) B500 and B) CNT_{ox} supports.

The larger macro-mesoporosity of the samples was characterized by mercury porosimetry while the narrowest meso-microporosity was studied by gas adsorption (Fig. 3 and Table 2). The pore size distributions (PSD) obtained by mercury porosimetry (Fig. 3A) point out that carbon aerogel B500 is a mesoporous sample, with a homogenous distribution of pores

with diameter around 10 nm whereas the Norit AC is a macroporous sample with pores with diameter around 700 nm. When analysing the N₂-sorption isotherms (Fig. 3B), it is observed that the Norit support presents however the greater microporosity pointed out by a fast increase in the adsorption capacity at low relative pressures (P/P₀); the isotherm is clearly type I typical of microporous samples. However, the large knee previous to the plateau pointed out certain heterogeneity in the microporosity as well the slight slope of the plateau the existence of certain mesoporosity. In the case of B500, the sorption isotherm is clearly type IV, corresponding to mesoporous samples, the slope of the plateau and the hysteresis cycle from P/P₀ > 0.6 denoting the presence of mesopores. The isotherm obtained for CNT_{ox} sample is mainly type III, denoting a weak interaction with the adsorbate. The micropore volume is quite low and the slope of the plateau and the hysteresis cycle, mainly at high relative pressures, also denotes the formation of certain mesoporosity. The application of the DFT method to analyse these isotherms allows to obtain the corresponding PSD, as showed in Fig. 3C. Results are consistent with those previously obtained by mercury porosimetry, B500 presenting again a monomodal PSD around pores of 10 nm of diameter, the PSD of CNT_{ox} being also quite similar, while in the case of the Norit AC the mesoporosity is scarce and the PSD profile is maxima for narrowest micropores. The PSD obtained for CNT_{ox} confirms that in general the mesoporosity corresponds to interparticle spaces formed into the CNT aggrupation,³⁸ considering that the internal diameter is clearly smaller than the mesopore size (between 2-50 nm) (see photos below).

When analysing the textural properties of the catalysts regarding their corresponding supports, it is observed a certain blockage of the narrowest microporosity by the metal nanoparticles, the PSD of macro and mesopores remaining practically unchanged. This is evidently related, therefore, with the metal loading and dispersion, which is in turn, influenced by the support and metal precursor nature as well the thermal treatment of activation. In Figure 3D is showed, as an example, the influence of the precursor on the textural properties of the catalysts. Although as commented, the microporosity decreases in both cases regarding the AC support, this blockage is stronger, for the same metal loading and pre-treatment, when using nitrate instead cobalt acetate. Nevertheless, both catalysts showed a similar hysteresis cycle at the same range of P/P₀ than those observed in the support, indicating that the mesoporosity is preserved. The textural characteristics of supports and catalyst derivatives are numerically summarized in Table 2. The study of the microporosity is also complemented by CO₂ adsorption, considering that this adsorbate can be adsorbed into the narrowest microporosity, i.e. in pores with diameter < 0.7 nm.³⁹ The higher surface values correspond to the Norit support as consequence of the high microporosity of this sample as above commented, while CNT_{ox} presents the lowest surface area value in spite to present the highest total pore volume, V_T. In all cases, the porosity of the

Dalton transactions

ARTICLE

Table 2. Porosity parameters of the samples.

Sample	S_{BET} (m^2/g)	S_{CO_2} (m^2/g)	$W_{0(\text{N}_2)}$ (cm^3/g)	$W_{0(\text{CO}_2)}$ (cm^3/g)	V_{T} (cm^3/g)
CNT _{ox}	339	121	0.14	0.10	2.08
CNT _{ox} 1Co	219	65	0.08	0.05	1.49
CNT _{ox} 3Co	228	41	0.09	0.04	1.45
CNT _{ox} 5Co	222	32	0.12	0.03	1.64
Norit	1233	621	0.54	0.27	0.61
Norit3CoAc	1147	765	0.31	0.48	0.60
Norit3Co	1050	696	0.27	0.44	0.54
B500	629	550	0.22	0.16	1.25
B5003Co	619	470	0.22	0.17	1.20

$W_{0(\text{N}_2)}$ = micropore volume and V_{T} = total volume both determined by N_2 adsorption. $W_{0(\text{CO}_2)}$ = micropore volume determined by CO_2 adsorption.

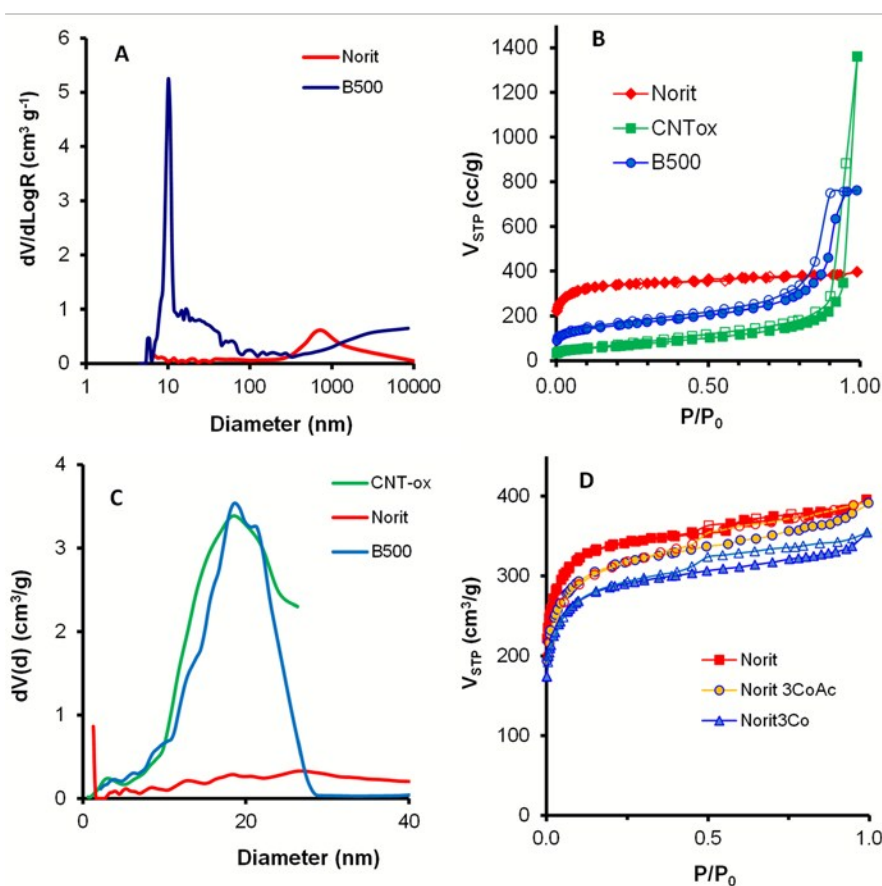


Fig.3 Porous characteristics of supports. A) PSD obtained by mercury porosimetry. B) N_2 -sorption isotherms (close symbol: adsorption open symbol: desorption branch). C) PSD obtained from N_2 -sorption isotherms by applying the DFT method. D) Influence of the metal precursor on the porosity of catalysts.

ARTICLE

catalysts changes regarding their supports, this feature being influenced by the location and distribution of the metallic particles, as detected in previous works.⁴⁰ Thus, when supported on CNT_{ox}, S_{BET} surface area values do not change with the Co-loading, even the micropore volume determined by N₂-adsorption increasing. The pore blockage in this case occurs inside the narrowest micropores, determined by CO₂-adsorption, W₀ (CO₂), which progressively decreased (Table 2). On the contrary, using Norit as support the stronger micropore blockage occurs in the larger microporosity, W₀ (N₂), and is stronger when using nitrate instead acetate, suggesting a different metal nanoparticle size. In this case, W₀ (CO₂) and consequently the S_{CO₂} surface area increase regarding the corresponding supports because the narrowest microporosity is enhanced due to the formation of metal nanoparticles inside the larger microporosity. The behaviour of B500 as support is clearly intermediate, because this material presents both a well-developed mesoporosity but also a significant microporosity allowing, therefore, the deposition of the metal particles on the large external surface of the mesopores and leading to a smaller reduction of the porosity.

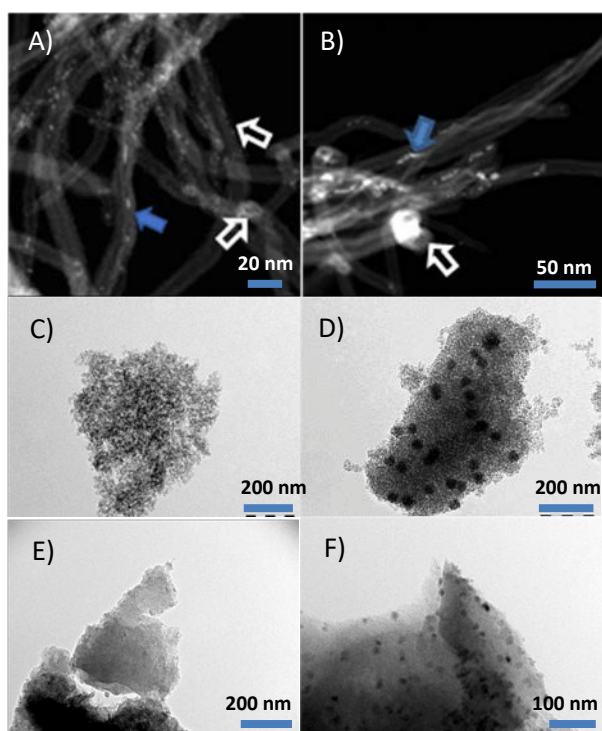


Fig. 4 HAADF-STEM images for A) CNT_{ox}3Co, B) CNT_{ox}5Co, and TEM images for C) B500-1Co, D) B500-5Co, E) Norit3Co and F) Norit3CoAc samples. Dense arrows point out small CoO-nanoparticles inside the pores whereas hollow arrows indicate those located at external surface.

The location and distribution of metallic nanoparticles (dispersion) on the different supports were analysed by HRTEM (Fig. 4). In the case of CNT_{ox}, the internal hollow is around 7 nm in diameter. Inside this porosity sometimes small Co-nanoparticles are placed (marked in the Fig. 4 with dense arrows) the most of them being located on the external surface of the CNTs (marked with hollow arrow).

The particle size distribution obtained for these samples are showed in Figure 5. Although in general external particles are bigger than those located inside the CNTs, many of them are also quite small but their particle sizes tend to increase with increasing the Co-loading. Thus, the distribution is shifted from particles with a typical diameter around 7 nm to particles of around 13 nm. The formation of larger particles exceeding the 20 nm were also observed, which also favor the CNTs grouping, this fact being related with the detected increase of W₀ (N₂).

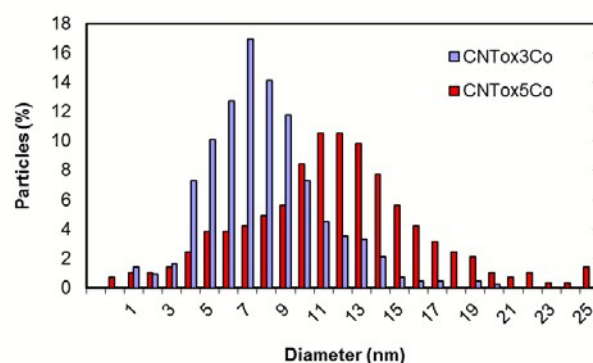


Fig. 5 Distribution of the nanoparticle size determined by HTREM for CNT_{ox}nCo.

As previously commented, the support B500 is composed by nearly spherical carbon particles that coalesce between them, forming a solid with high mesopore volume between these primary particles and giving a granulated aspect to the support. The high external surface associated to these mesopores makes it an appropriated support to develop highly dispersed catalysts, in such a manner that Co-particles are quite difficult to be distinguished at low Co-loading (Fig. 4C) barely influencing the porous texture. Nevertheless, sintering increases at high Co-loading (Fig. 4D). The Norit AC is denser but shows large micropores allowing a very high dispersion of Co-nanoparticles. It is important to stress that the Co-particle size increases when use acetate instead nitrate salt (Fig. 4E and 4F). However, even in the worst case, well distributed nanoparticles with diameter of around 13 nm were obtained.

Similar information is also obtained by EDX-mapping of different areas of the catalysts (Fig. 6), the images showing the good and homogeneous dispersion of Co on the CNTs surface.

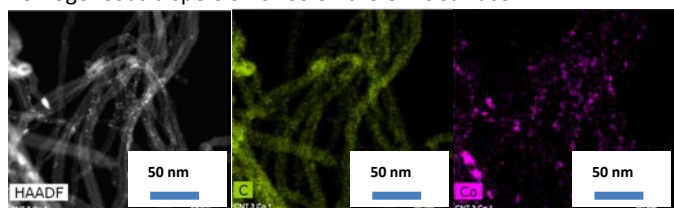


Fig. 6 EDX-Mapping of Co-species on the CNTs (CNT_{ox}3Co).

Although the Co-nanoparticles reach a significant size in some samples, their XRD patterns do not present any diffraction peaks associated to the Co-phase. At this regard, we try to identify the chemical nature of the metallic particles and the interactions with the supports by XPS analysis of the samples. Thus, the oxygen, carbon and cobalt spectral regions were analysed (Table 3). The peak C1s at the carbon region was fitted using four components. The first one at 284.9 eV corresponding to aromatic and aliphatic carbon, while the other ones are associated to the presence of heteroatoms; the component at 286.5 eV corresponding to single C-O bonds, the component at 288 eV to C=O and finally the carbonate species at around 290 eV. The oxygen region O1s is fitted using two components, the first one at around 532 eV associated to C=O bonds and the second one at 533 eV corresponding to C-O bonds. Although this region is fitted also using only two components, clearly the component at low B.E. is favoured after impregnation, due to the contribution of oxygen linked to the metal nanoparticles. Consequently, the oxygen content also significantly increases. The atomic Co-content on surface is 5.8%, corresponding to a 18.4% wt. This value is clearly higher than the nominal loading (3%) indicating that the metal is well dispersed only on the high external surface of the support. The analysis of the Co-spectral region is notably more difficult⁴¹ due to the presence of shake-up satellites together with the Co(2p_{3/2}) and Co(2p_{1/2}) photolines (Fig. 7). The components at 781.9 eV Co(2p_{3/2}) and 797.7 eV Co(2p_{1/2}) with the satellite at 787.1 eV suggest the presence of Co^{II}, probably as oxide /hydroxide species.⁴²

The existence of oxidized Co-species on the catalysts surface is also pointed out by TG-DTG experiments carried out in He flow (Fig. 8). Comparing this result with those previously presented for the supports in Fig. 1C, it is noteworthy the new significant peak at around 640 K, that progressively increases with increasing the metal loading. This peak is associated to the WL produced by the reduction of the Co oxide/hydroxide by the carbon matrix, evolving CO_x.

Interestingly, it is important to remark that these catalysts significantly differ from those previously developed and used in the reaction under study.^{22,23} Previous Co-catalysts were prepared by metal-doping during the sol-gel synthesis of the carbon aerogel, and thereafter carbonized at high temperature (1273 K), therefore metal particles were reduced to Co⁰ during the thermal treatment. In this case, carbon catalysts are prepared by impregnation, metal particles formed exclusively on the support surface during a soft thermal treatment at 573 K. In such a way, amorphous nanoparticles remaining as cobalt oxides/hydroxides are obtained,

which should present therefore also a different catalytic performance as showed below.

DOI: 10.1039/C8DT04403A

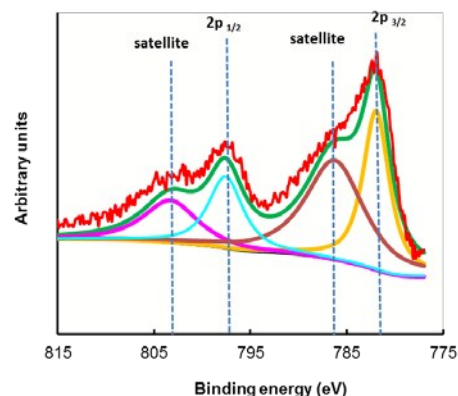


Fig. 7 Fitting the XPS spectral region of Co in the B5003Co catalysts.

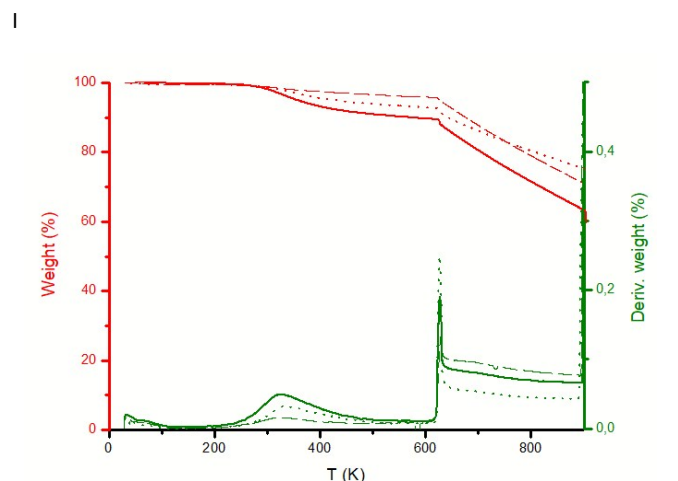
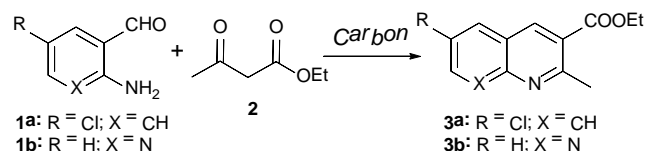


Fig. 8 TG-DTG of CNT_{ox}1Co (---), CNT_{ox}3Co (—) and CNT_{ox}5Co (•••) catalysts in He flow.

Catalytic performance

First, the catalytic performance of the investigated nanocarbons used as supports was checked on the condensation of 2-amino-5-chlorobenzaldehyde (**1a**) and ethyl acetoacetate (**2**) for the synthesis quinolines **3a** (Scheme 1) as an analogue of biologically relevant compound.⁴³ As demonstrated in our previous studies, the carbon support is active in the reaction when operating at 323 K, producing the quinoline **3a** in low yields probably involving π,π -stacking interactions.²¹



Scheme 1 Friedländer condensation from 2-aminoaryl aldehydes (**1**) and ethyl acetoacetate (**2**), under solvent-free conditions.

ARTICLE

Table 3. Atomic Surface composition (by XPS) and Binding Energy of B500 support and B5003Co catalyst.

Sample	C (at%)	O (at%)	Co(at%)	B.E. C (eV)	B.E. O (eV)	B.E. Co (eV)
B500	92.8	7.2	-	284.9 (74%)	531.9 (24%)	--
				286.5 (18%)	533.8 (76%)	
				288.8 (6%)		
				290.8 (2%)		
B5003Co	72.6	21.6	5.8	284.8 (73%)	531.5 (41%)	781.9 (100%)
				286.3 (16%)	533.6 (59%)	
				288.2 (6%)		
				289.5 (5%)		

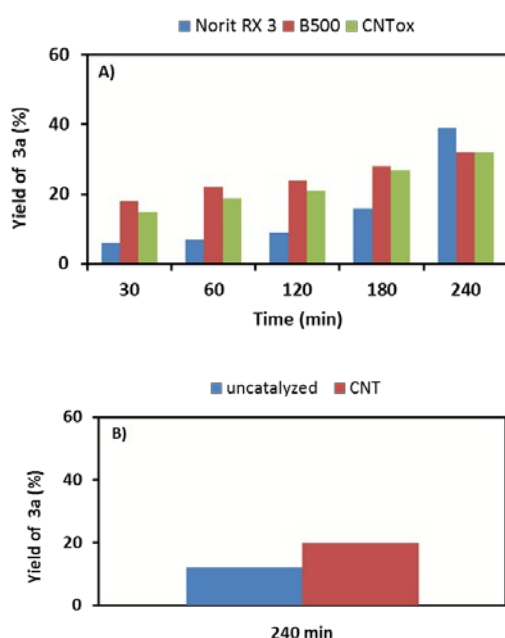
**Fig. 9** Friedländer condensation from 2-amino-5-chlorobenzaldehyde (**1a**) and ethyl acetoacetate (**2**) catalysed by nanocarbons, at 323 K, under solvent-free conditions.

Fig. 9A depicts the comparison of yield vs time for the carbon supports Norit, B500 and CNT_{ox} when operating at 323 K exhibiting notable differences at the shortest reaction times. In these cases, the porosity of the samples seems directly affect to the reactivity, the presence of the mesopores in B500 leading to increased yields of compound **3a**. Similar trend was observed for the CNT_{ox} regarding B500 sample. In this case, the smaller surface can be compensated by large interparticle volume and the presence of OSG generated during the acid treatment, which could be also responsible of the selective formation of quinoline **3a** together π , π -stacking interactions between catalysts and reactant as accounted

for the previous reported studies concerning the oxygenated carbon materials.²¹ The reaction in the presence of Norit RX3, a mainly microporous sample, led to the quinoline **3a** in notably decreased yields, at the shortest reaction times, due to the diffusion delays into the micropores, but become the most active support at prolonged time on stream probably because this support shows the highest surface area. In Figure 9B, it is shown the yield of quinoline **3a** after 4 h of reaction time for both the uncatalyzed reaction (12%) and in the presence of raw CNT (20%) for comparison purposes.

The reaction under the same experimental conditions used above and in the presence of the Co-supported nanocarbons afforded the quinoline **3a** in almost quantitative yields after 15 min of reaction time. Then, CoO nanoparticles supported over the carbon surface notably increased the yields of **3a**. Remarkably CoO is now the catalytic specie, much more active than the Co⁰ nanoparticles.²²

Having these results in mind, we carried out the reaction notably increasing the reagent molar ratio (2:5 vs 0.5:5) but also decreasing the reaction temperature, operating at temperature close to room temperature, 303 K. The catalytic behaviour of the samples based on mesoporous nanocarbons by varying the concentration of the active phase is summarized in Fig. 10. For the carbon aerogel-based catalysts, it was observed an increment of yield of **3a** as function of the concentration of Co active phase in such a manner that the B5005Co sample led to compound **3a** with increased yields. However, at short reaction times this catalyst is slower than B5003Co, probably associated to the worse dispersion of the active phase previously showed. This behaviour is even more significant in the CNT_{ox}nCo serie in which it seems that the CNT_{ox}3Co nanocarbon shows the optimal amount of CoO exhibiting the highest yields to product. Regarding to that, the CNT_{ox}1Co and NTC_{ox}5Co samples showed a similar catalytic behaviour affording the quinoline **3a** with almost identical yields. In these cases, the highest metal content distributed over the lowest surface area of CNT_{ox} also produce the formation of CoO aggregates as demonstrated by the HRTEM images. The effect of the porosity and the nanoparticles location is

even more noticeable at intermediate metal loadings (Fig. 10). CoO supported on B500 are faster than when supported on CNTs, in this case favoured by a high dispersion degree (Fig. 4C). Thus, although B5003Co and CNT_{ox}3Co afforded the quinoline **3a** in high yields after 1h of reaction time (up to 60%), at short reaction times (15 min) B5003Co sample yielded the quinoline **3a** in 72% vs 37 and 16% for the CNT_{ox}3Co and Norit3Co samples, respectively (Fig. 11), this feature demonstrating the advantage of using carbon aerogels.

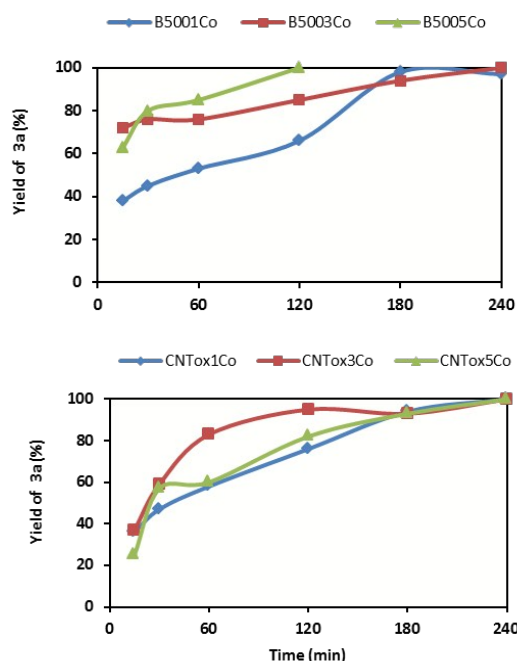


Fig. 10 Friedländer condensation from 2-amino-5-chlorobenzaldehyde (**1a**) and ethyl acetoacetate (**2**) catalysed by CoO-supported nanocarbons –B500nCo and CNT_{ox}nCo series – at 303 K, under solvent-free conditions.

This figure clearly pointed out the importance of the location of the active phase and in turn of the support porosity. Thus, the worse initial performance of CoO supported on microporous carbon Norit is evidently associated to the delay caused by the diffusion of reactants and products to the catalytic sites, as commented, while the best performance was observed for the highly mesoporous carbon aerogel. The CNT_{ox}nCo serie exhibited an intermediate catalytic behaviour, probably due to the Co-nanoparticles distribution on both the internal and external surface of the nanotubes. Conversion increases slowly in the case of B500nCo catalysts with the reaction time because the concentration of the reactants strongly decreases in the first stage. However, in both CNT_{ox}nCo and NoritnCo series, the Co-nanoparticles inside the pores became progressively active as they were located in deeper and narrower porosity. Conversion increased faster in the case of CNTs because the internal diameter is of around 7 nm (mesopores) regarding the micropores present in the Norit support. Nevertheless, this sample became finally the most active due to the higher catalytic surface and high Co-dispersion.

The impregnation salt nature has a deep impact on the location of the Co-nanoparticles as previously commented. The metal dispersion decreases when using Co(CH₃CO₂)₂ instead Co(NO₃)₂ (Fig.

4). When supported on CNT_{ox} (Fig. 12) it is observed that in spite the loss of the active site numbers by the stronger sintering, CNT_{ox}3CoAc catalyst is more active than CNT_{ox}3Co. When use the microporous activated carbon Norit as support, Norit3CoAc is more active than Norit3Co, especially at the shortest reaction times, but the activity of the later improve with the reaction time. This is again related with the accessibility of reactants to the active phase, thus, the large nanoparticles from the acetate precursor are formed progressively out of the microporous system of the support being more active at short reaction times while with increasing this parameter the best performance is observed for the small nanoparticles located inside the pores. Therefore, the used metal precursor in the catalyst synthesis also influences the catalytic performance and the relationship between particle size and location should be therefore optimized to obtain fast, selective and stable catalysts. Finally, remark that CNT_{ox}3CoAc was reused during five times with only a slight activity loss (80, 79, 72, 74 and 71 % after 15 min of reaction time).

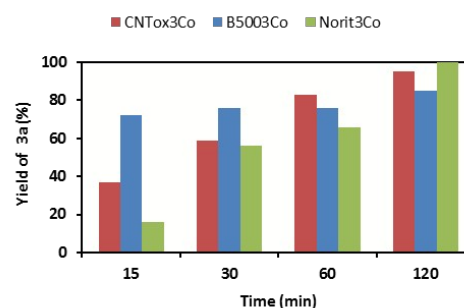


Fig. 11 Friedländer condensation from 2-amino-5-chlorobenzaldehyde (**1a**) and ethyl acetoacetate (**2**) catalysed by CoO-supported nanocarbons – B5003Co, CNT_{ox}3Co and Norit3Co – at 303 K, under solvent-free conditions.

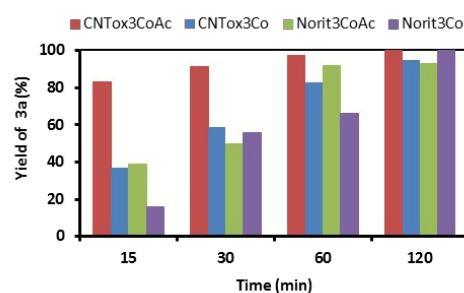


Fig. 12 Friedländer condensation from 2-amino-5-chlorobenzaldehyde (**1a**) and ethyl acetoacetate (**2**) catalysed by CoO-supported nanocarbons – CNT_{ox}3CoAc and Norit3CoAc – at 303 K, under solvent-free conditions.

In addition, we study the reaction using 2-aminonicotinaldehyde (**1b**) and ethyl acetoacetate (**2**) catalyzed by CNT_{ox}3CoAc (Scheme 1). Fig. 13 depicts the yield of **3b** vs time in the presence of CNT_{ox}3CoAc, at 303 K, observing a pronounced decay of yield compared to when using benzaldehyde **1a**, as expected according our previous results. This circumstance suggests a lower reactivity

Dalton transactions

ARTICLE

Table 4. Performance of the investigated catalysts.

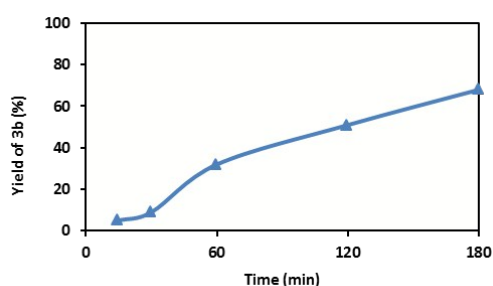
Catalyst	TEM D(nm)	Dispersion (%)	Conversion (%)	TOF (s ⁻¹)	R (mmol/g Co · s)
CNT _{ox} 1Co	2	48.0	36	0.40	3.20
CNT _{ox} 3Co	8	12.0	37	0.55	1.10
CNT _{ox} 5Co	13	7.4	25	0.36	0.44
Norit3Co	2	48.0	16	0.06	0.47
Norit3AcCo	9	10.7	39	0.65	1.16
B5001Co	10	9.6	38	2.11	3.38
B5003Co	20	4.8	72	2.66	2.13
B5005Co	30	3.2	63	2.10	1.12

*Conversion values after 15 min. ** Total selectivity to **3a** is obtained.

Table 5. Catalysts reported for the Friedländer reaction from 2-aminoaryl aldehydes (**1**) and ethyl acetoacetate (**2**).

Catalyst	Reaction product	Reaction Conditions	Time (min)	Yield (%)	Ref.
PET/MAG	3a	1a (0.5 mmol), 2 (5mmol), catalyst (25 mg), 293 K	60	71	20
RFCoS	3a	1a (0.5 mmol), 2 (5mmol), catalyst (25 mg), 323 K	60	93	22
Cu-BTC	3a	1a (0.5 mmol), 2 (5mmol), catalyst (25 mg), 323 K	60	58	22
B5003Co	3a	1a (2 mmol), 2 (5mmol), catalyst (25 mg), 303 K	15	71	This work
CNT _{ox} 3CoAc	3a	1a (2 mmol), 2 (5mmol), catalyst (25 mg), 303 K	15	86	This work
B5003Co	3a	1a (2 mmol), 2 (5mmol), catalyst (25 mg), 303 K	15	73	This work
CNT _{ox} 3CoAc	3b	1b (2 mmol), 2 (5mmol), catalyst (25 mg), 303 K	120	51	This work
AP/Al-MCF	3b	1b (0.5 mmol), 2 (5mmol), catalyst (25 mg), 323 K	120	42	44

probably due to the acid-base strong interactions of both reactant **1b** and product **3b** with active catalytic sites²⁰.

**Fig. 13** Friedländer condensation from 2-aminonicotinaldehyde (**1b**) and ethyl acetoacetate (**2**) catalyzed by CNT_{ox}3CoAc, at 303 K, under solvent-free conditions.

The performance of the investigated catalysts was compared also in terms of specific activity, R – (mmol/g(Co) s) – and turn over frequencies, TOF – (mol **1a** converted/mol surface-Co·s) – (Table 4). As previously explained, the Co-particle size depends on different factors like metal loading, precursor, etc, which together with location of these nanoparticles inside the porosity influence the catalytic performance previously described. Table 4 summarizes the

catalytic performance of different catalysts series showing this effect, comparing the activity in terms of Co-loading (specific activity) or surface-Co sites (TOF). In this case, dispersion clearly decreased with Co-loading, and conversion values even decreased. Evidently this is also translated to a decrease in the reaction rate (R, mmol/g Co · s). However, the TOF values are quite similar between samples, denoting similar character of the active sites and a similar accessibility to reactants, because Co-particles are formed mainly on the external surface of the CNT. These means that the number of active sites only increased slowly from 1 to 3% loading, but significantly decreased for 5%-Co. A similar effect is observed for the catalysts series supported on the mesoporous aerogel B500. When using microporous support and different Co-precursors, it is clearly observed a best dispersion using nitrate than acetate (Figures 4E and 4F). However, the conversion values are higher when using acetate showing a greater activity either in terms of R or TOF. This is clearly indicative of the importance of the particle location. While Co-nanoparticles from nitrate can be formed inside the largest micropores (of around 2 nm of diameter), when using acetate the nanoparticles (9 nm of diameter) are forced to be formed into the mesoporosity; Co-nanoparticles consequently becoming more accessible to the reactants than the smaller one located in the narrowest porosity. Nevertheless, as commented

above, although the different kinetics of the process, total conversions are obtained in all cases with increasing the time on stream.

Concerning the reaction mechanism for the investigated condensation, when using Co⁰ doped carbon aerogels we previously proposed the *in situ* generation of Co⁰-Co^{II} catalytic system, which would initiate the condensation reaction between reactants.^{22,23} The enhanced catalytic performance observed for the nanocarbons herein reported is then attributed to the presence of CoO. Based on our experience, CoO could act as dual catalyst in which O atom would activate the ethyl acetoacetate, through its enol form, whereas Co increasing the electrophilic character of the carbonyl acceptor strongly favouring the reaction. Subsequent heterocyclization followed by double dehydration steps would yield the corresponding quinoline.

Finally, Table 5 summarizes the catalysts described for the synthesis of quinolines **3**, demonstrating the high potential of CoO supported carbon catalysts under study. These catalytic materials were found to be easily prepared as a sustainable alternative to metal organic frameworks (MOFs), particularly Cu-BTC, bifunctional mesoporous silicas (AP/AIMCF) and even other basic carbocatalysts with high metal oxide loadings (PET/MAG).

Conclusions

We report herein the first examples of CoO supported on carbon nanomaterials highly efficient in the synthesis of nitrogen heterocyclic compounds through the Friedländer condensation, under solvent-free and mild conditions. Three series of eco-sustainable catalysts, exhibiting enhanced catalytic performance are prepared and characterized and these properties related with their catalytic performance. The support (AC, CNT or carbon aerogels) porosity and surface chemistry influence the formation of CoO nanoparticles on different porosity ranges. The size and distribution of these nanoparticles are also influenced by the Co-precursor salt. Sintering increased with increasing the metal loading. In the case of mesoporous aerogels the nanoparticles can be located in the mesoporosity and large micropore range, favouring a homogeneous distribution and the accessibility of reactants (fast reactions). On the contrary, although microporous ACs with high specific surface area induce slowly the reaction, conversion increasing with the reaction time, yields to **3a** were even greater than in the previous case. When using CNT_{ox}, in spite that present the highest pore volume, some of the metal nanoparticles are formed inside the nanotubes, showing an intermediate behaviour between mesoporous carbon aerogels and microporous ACs. Among the explored samples, B5005Co was found to be the most efficient catalyst providing highest conversions to product, at the shortest reaction times, demonstrating the advantage of using mesoporous carbon aerogels as pure carbon support. The CoO-carbon based catalysts herein reported are found to be much more efficient than MOFs, bifunctional mesoporous silicas and even basic carbon catalysts, showing also a notable stability along different reaction cycles. Then, these interesting results open the doors to the development of functional carbon aerogels

able to efficiently catalyse the synthesis of relevant heterocyclic systems through cascade reactions.

Conflicts of interest

There are no conflicts to declare.

Acknowledgements

This work has been supported by Spanish Ministry (CTM 2014-56668-R project).

Notes and references

- J. L. Figueiredo, Nanotechnology in Catalysis: Applications in the Chemical Industry, Energy Development, and Environment Protection, in: B. Sels, M. Van de Voorde (Eds.), Application of Nanocarbon Materials to Catalysis, Wiley-VCH Verlag GmbH & Co, KGaA, 2017, pp. 37–55.
- P. Serp and J. L. Figueiredo, Carbon Materials for Catalysis, John Wiley & Sons, Hoboken, NJ, 2009.
- E. Pérez-Mayoral, V. Calvino-Casilda and E. Soriano, *Catal. Sci. Tech.*, 2016, **6**, 1265–1291.
- F. Rodríguez-Reinoso, *Carbon*, 1998, **36**, 159–175.
- F. J. Maldonado-Hódar, *Catal. Today*, 2013, **218**, 43–50.
- Y. Yıldız, I. Esirden, E. Erken, E. Demir, M. Kaya, F. Sen, *Chem. Select*, 2016, **1**, 1695–1701.
- A. B. Dongil, B. Bachiller-Baeza, I. Rodríguez-Ramos, J. L. G. Fierro and N. Escalona, *RSC Adv.*, 2016, **6**, 26658–26667.
- P. Basu, P. Prakash, E. Gravel, N. Shah, K. Bera, E. Doris, I. N. N. Namboothiri, *ChemCatChem*, 2016, **8**, 1298–1302.
- J. John, E. Gravel, A. Hagège, H. Li, T. Gacoin and E. Doris, *Angew. Chem. Int. Ed.*, 2011, **50**, 7533–7536.
- R. Kumar, E. Gravel, A. Hagège, H. Li, D. V. Jawale, D. Verma, I. N. N. Namboothiri, E. Doris, *Nanoscale*, 2013, **5**, 6491–6497.
- N. Shah, E. Gravel, D. V. Jawale, E. Doris, I. N. N. Namboothiri, *ChemCatChem*, 2015, **7**, 57–61.
- Z. Hasan, Y. S. Ok, J. Rinklebe, Y. F. Tsang, D.-W. Cho, H. Song, *J. Alloys Compounds*, 2017, **703**, 118–124.
- M. Biegun, X. Chen and E. Mijowska, *ChemElectroChem*, 2018, **5**, 2681–2685.
- M. Hu, Z. Yao, X. Wang, *Ind. Eng. Chem. Res.*, 2017, **56**, 3477–3502.
- Y. Cheng, Y. Fan, Y. Pei, M. Qiao, *Catal. Sci. Technol.*, 2015, **5**, 3903–3916.
- D. Marquardt, C. Vollmer, R. Thomann, P. Steurer, R. Mülhaupt, E. Redel, C. Janiak, *Carbon*, 2011, **49**, 1326–1332.
- Z. Wei, Y. Chen, J. Wang, D. Su, M. Tang, S. Mao, Y. Wang, *ACS Catal.*, 2016, **6**, 5816–5822.
- J. Marco-Contelles, E. Pérez-Mayoral, A. Samadi, M. C. Carreiras, E. Soriano, *Chem. Rev.*, 2009, **109**, 2652–2671.
- J. López-Sanz, E. Pérez-Mayoral, E. Soriano, D. Omenat-Morán, C. J. Durán, R.M. Martín-Aranda, I. Matos, I. Fonseca, *ChemCatChem*, 2013, **5**, 3736–3742.
- M. Godino-Ojer, A. J. López Peinado, R. M. Martín Aranda, J. Przepiorski, E. Pérez-Mayoral, E. Soriano, *ChemCatChem*, 2014, **6**, 3440–3447.
- M. Godino-Ojer, E. Soriano, V. Calvino-Casilda, F. J. Maldonado-Hódar, E. Pérez Mayoral, *Chem. Eng. J.*, 2017, **314**, 488–497.
- M. Godino-Ojer, A. J. López Peinado, F. J. Maldonado-Hódar, E. Pérez-Mayoral, *ChemCatChem*, 2017, **9**, 1422–1428.

ARTICLE

Journal Name

- 23 M. Godino-Ojer, R. M. Martín-Aranda, F. J. Maldonado-Hódar, A. F. Pérez-Cadenas, E. Pérez-Mayoral, *Mol. Catal.*, 2018, **445**, 223–231.
- 24 M. Trépanier, A. Tavasoli, A. K. Dalai, N. Abatzoglou, *Appl. Catal. A*, 2009, **353**, 193–202.
- 25 F. J. Maldonado-Hódar, C. Moreno-Castilla, J. Rivera-Utrilla, M. A. Ferro-García, *Stud. Surf. Sci. Catal.*, 2000, **130B**, 1007–1012.
- 26 M. M. Dubinin, Chemistry and Physics of Carbon, in: P. L. Walker, Jr. (Ed), Marcel Dekker, New York, 1966. Vol. 2, pp. 51–120.
- 27 R.C. Bansal, J.B. Donnet, H.F. Stoeckli, Active Carbons, Marcel Dekker, New York. 1988.
- 28 A. V. Neimark, Y. Lina, I. Peter, P. I. Ravikovitch, M. Thommes, *Carbon*, 2009, **47**, 1617–1628.
- 29 F. Duarte, F. J. Maldonado-Hodar, L. M. Madeira, *Appl. Catal. B: Env.*, 2011, **10**, 109–115.
- 30 Q. Cheng, N. Zhao, S. Lyu, Y. Tian, F. Gao, L. Dong, Z. Jiang, J. Zhang, N. Tsubaki, X. Li, *Appl. Catal. B*. 2019, DOI: <https://doi.org/10.1016/j.apcatb.2019.02.024> (in press)
- 31 A. Martínez, C. López, F. Márquez, I. Díaz, *J. Catal.*, 2003, **220**, 486–499.
- 32 B. Zeng, B. Hou, L. Jia, J. Wang, C. Chen, D. Li, Y. Sun, *Catal. Sci. Technol.* 2013, **3**, 3250–3255.
- 33 T. W. van Deelen, J. J. Nijhuis, N. A. Krans, J. Zečević, K. P. de Jong, *ACS Catal.* 2018, **8**, 10581–10589.
- 34 C. S. D Rodrigues, R. M Silva, S. A. C. Carabineiro, F. J Maldonado-Hódar, L. M. Madeira, *J. Chem. Technol. Biotechnol.* 2018, **93**, 3223–3232.
- 35 F. J. Maldonado-Hódar, M. A. Ferro-García, J. Rivera-Utrilla, C. Moreno-Castilla, *Carbon*, 1999, **37**, 1199–1205.
- 36 J. L. Figueiredo, M. F. R. Pereira, M. M. A. Freitas, J. J. M. Orfao, *Carbon*, 1999, **37**, 1379–1389.
- 37 J. F. Vivo-Vilches, E. Bailón-García, A. F. Pérez-Cadenas, F. Carrasco-Marín, F. J. Maldonado-Hódar, *Carbon*, 2014, **68**, 520–530.
- 38 Q. H. Yang, P. X. Hou, S. Bai, M. Z. Wang, H. M. Cheng. *Chem. Phys. Lett.*, 2001, **345**, 18–24.
- 39 D. Cazorla-Amoros, J. Alcañiz-Monge, M. A. De la Casa-Lillo, A. Linares-Solano, *Langmuir*, 1999, **14**, 4589–4596.
- 40 F. M. Duarte, F. J. Maldonado-Hódar, L. M. Madeira, *Appl. Catal. A*, 2013, **458**, 39–47.
- 41 C. Moreno-Castilla, F. J. Maldonado-Hódar, A. F. Pérez-Cadenas, *Langmuir*, 2003, **19**, 5650–5655.
- 42 Z. Kónya, J. Kiss, A. Oszkó, A. Siska, I. Kiricsi, *Phys. Chem. Chem. Phys.*, 2001, **3**, 155–158.
- 43 P. Ornaghi, D. Rotili, G. Sbardella, A. Mai, P. Filetici, *Biochem. Pharmacol.*, 2005, **70**, 911–917.
- 44 A. Smuszkiewicz, E. Pérez-Mayoral, E. Soriano, I. Sobczak, M. Ziolk, R. M. Martín-Aranda, A. J. López-Peinado, *Catal. Today*, 2013, **218–219**, 70–75.

View Article Online
DOI: 10.1039/C8DT04403A

Dalton Transactions Accepted Manuscript